Aircraft Wake Detection Using Bistatic Radar: Analysis of Experimental Results

Russell J. Iannuzzelli, Charles E. Schemm, Frank J. Marcotte, Laurence P. Manzi, Harold E. Gilreath, James M. Hanson, Jr., David A. Frostbutter, Alexander S. Hughes, Allen D. Bric, Dennis L. Kershner, and Leo E. McKenzie

The Applied Physics Laboratory has built and fielded an experimental bistatic X-band continuous-wave radar system for studies in aircraft wake vortex detection. The radar, along with an acoustic pumping system, was installed at the Baltimore-Washington International Airport in the fall of 1996. Controlled experiments using a NASA C-130 aircraft were conducted on 23 September, 29 October, and 10 December. Results from two specific runs on 29 October are presented and discussed along with numerical simulations of those runs.
(Keywords: Bistatic radar, Radioacoustic sounding, Wake vortex.)

INTRODUCTION

Wake vortices produced by the lifting surfaces of large commercial transport aircraft can have catastrophic effects on smaller planes following closely behind. Many incidents have been blamed on wingtip vortices in the past 15 years. The Federal Aviation Administration (FAA) and NASA are working with industry to develop an intelligent system called the Aircraft Vortex Spacing System. This system would determine the optimum aircraft spacing within 3.2 km of each runway based on a combination of vortex sensors located near the glide slope and a real-time predictive model of the vortex environment in the atmosphere. The sensors would be used initially to validate this model. A vortex detection system such as this would not only enhance airport productivity by allowing adaptive spacing, but would increase the safety of all aircraft operating around the airport by alerting controllers that hazardous conditions may exist near the runways.

In 1996, APL initiated an internal research project to investigate the usefulness of a bistatic X-band continuous-wave radar system for detecting wingtip vortices around the end of a runway. The bistatic radar, built by APL, was installed at the Baltimore-Washington International Airport (BWI) on either side of the south end of runway 33L. Data were taken on a C-130 emitting smoke from the wingtips on 23 September, 29 October, and 10 December 1996. In addition to the radar, an acoustic illumination system was built and installed to evaluate acoustic pumping for possible signal detection enhancement.

A previous article on the vortex detection radar appeared in the *Technical Digest* in 1997.[1] This second article gives an expanded view of the acoustic illumination and radioacoustic detection as well as the receiver processing. In addition, we present and analyze results from both the BWI experiments and several simulation runs from the APL-developed Wake Evolution Code (AWEC).

INSTRUMENTATION RADAR DESIGN ANALYSIS

The weather radar range equation for estimating received power P_R for a continuous-wave bistatic radar,

in which the transmitter and receiver are spatially separated, can be shown to be

$$P_R = \frac{P_T G_T G_R \lambda^2}{(4\pi)^3 R_T^2 R_R^2} \eta_v (V_C \cap V_V), \quad (1)$$

where

P_T = transmitter power,
G_T and G_R = transmitter and receiver antenna gains, respectively,
λ = wavelength,
R_T and R_R = ranges from the transmitter and receiver to the intersection of the two antenna beams, respectively,
η_v = reflectivity of volume clutter (expressed in m^2/m^3),
V_C = the common volume, which is contained within the intersection of the transmitter's and receiver's conical beams, and
V_V = vortex volume.

For a monostatic radar, the ranges are identical.

From Ref. 2, clear air turbulence reflectivity η_v can be expressed as

$$\eta_v = 2\pi k^4 \Phi[2k \sin(\theta_S/2)], \quad (2)$$

where $k = 2\pi/\lambda$ is the radar wavenumber, and θ_S is the scattering angle, i.e., the angle at which the radar energy is bent at the common volume from the transmitter toward the receiver (180° for the monostatic case). The spectral representation of the turbulence is given by

$$\Phi(\kappa) = 0.033 C_n^2 \kappa^{-11/3}, \quad (3)$$

where κ is the spatial wavenumber, and C_n^2 is a structure parameter that measures the intensity of turbulent fluctuations. For the special case of homogeneous isotropic turbulence, C_n^2 can be expressed in terms of the more general structure $D_n(r)$ using

$$C_n^2 = r^{-2/3} D_n(r), \quad (4)$$

where

$$D_n(r) \equiv \overline{[n(x+r) - n(x)]^2} \quad (5)$$

is the structure function, and r is a spatial increment. The variable n in Eq. 5 is the refractive index of air, which is related to meteorological variables (temperature, pressure, humidity). The overbar indicates an ensemble average. Values of C_n^2 can range from 10^{-16} $m^{-2/3}$ for weak turbulence to 10^{-12} $m^{-2/3}$ for very strong turbulence.[3,4]

Vortex detection by radar poses several challenges to the radar designer. Most of the problems arise because the vortex provides little radar return. Since most of the refraction will be away from the radar transmitter (Ref. 1), a bistatic arrangement is favored. The biggest problem with the bistatic continuous-wave radar is the performance degradation due to phase noise from the spillover signal. Unlike pulse radars, a continuous-wave radar is both transmitting and receiving all the time. Time gating, which isolates a pulse radar receiver from the transmitter, does not apply with a continuous-wave radar, so other means of isolating the high spillover signal from the transmitter into the receiver must be used. We applied several techniques to reduce spillover at BWI, including construction of fences around the transmitter and receiver shelter and separation and pointing of the receiver/transmitter so that sidelobe patterns could help null out as much of the direct spillover as possible. In addition, we experimented with an active nuller[1] and adaptive processing, which will be described later in this article. Figure 1 depicts a hypothetical received signal spectrum, with a finite-passband noiselike vortex signal component, a receiver noise component, and a spillover component with phase noise.

RADIOACOUSTIC DETECTION OF AIRCRAFT WAKES: ACOUSTIC PUMPING

In 1961, the Midwest Research Institute developed a radioacoustic detection system, later known as RASS (radioacoustic sounding system), as a means for measuring the temperature profile of the lower

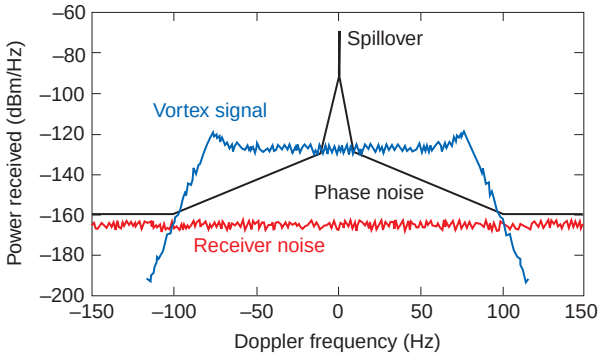

Figure 1. Illustration of received vortex signal spectrum showing the major components. Turbulent fluctuations, C_n^2, were 10^{-12}, 10^{-14}, and 10^{-16} $m^{-2/3}$ for strong, moderate, and weak turbulences, respectively. Radar specifications were transmitter power = 400 W, beamwidth = 1.6°, transmitter/receiver separation = 1620 m, and vortex height = 61 m.

atmosphere.[5] The method was later refined and extended elsewhere, notably at Stanford University,[6,7] in the former Soviet Union,[8–10] and most recently in Norway.[3] In such a system, acoustic waves are transmitted into the atmosphere to produce traveling perturbations in the index of refraction that can be sensed by a bistatic radar. The design depends on establishing the Bragg scattering condition, in which the RF energy that is scattered from successive acoustic wavefronts adds coherently at the receiver. For a simple collinear configuration, with the transmitter and receiver equidistant from the acoustic source (cf. Fig. 2), this condition occurs when

$$k_a = 2k \sin(\theta_S / 2), \tag{6}$$

where k_a is the acoustic wavenumber.

By virtue of the movement of the scattering wavefronts, the frequency of the received RF signal is shifted by an amount equal to the Doppler frequency f_d, which, for a quiescent atmosphere, equals the frequency of the acoustic source f_a:

$$f_d = f_a = -k_a v_s, \tag{7}$$

where v_s is the sound speed. A change in the speed of the wavefronts, which can be due to the advection of the waves by air currents or by a variation in sound speed, changes the Doppler frequency, and tracking this change is the basis for measuring wind speed or temperature.

An idealized version of a radioacoustic system has been analyzed[2] for the case of Fraunhofer scattering from advecting perturbations in the refractive index. Applying this analysis to the configuration shown in Fig. 2, and arranging the results in the form of the bistatic radar equation, we obtain

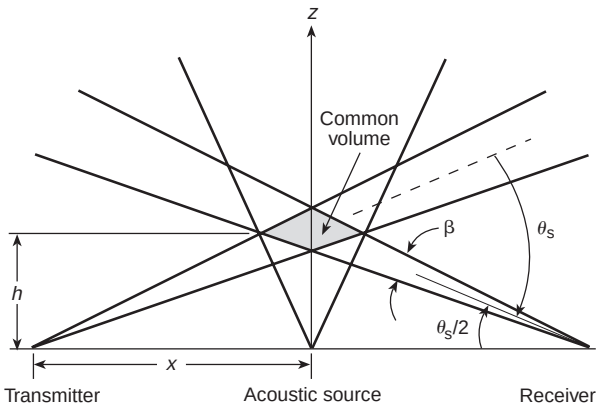

Figure 2. Radioacoustic detection of aircraft vortices (θ_S = scattering angle, β = antenna beamwidth, and h = height.)

$$P_r = \left\{\left(P_T g^2 \lambda^2\right) / \left[\left(4\pi\right)^3 R^4\right]\right\}\sigma, \tag{8}$$

where P_r = echo power, g = antenna gain, and R = range.

The variable σ is an effective cross section (radar cross section of the entire volume), which is shown to be

$$\sigma = C\left\{\left(P_a g_a k^4\right) / \left[\left(4\pi\right)^2 h^2\right]\right\}, \tag{9}$$

where P_a is the power of the acoustic source, g_a is the acoustic antenna gain, h is the distance from the acoustic source to the center of the common volume, the constant C is given by

$$C = 2(K\rho)^2/(\rho v_s^3) \approx 3.69 \times 10^{-15}\ \mathrm{m^2/W}, \tag{10}$$

and K is the Gladstone-Dale constant (see the boxed insert).

For the radioacoustic configuration used in the BWI experiments, the acoustic line in the Doppler spectrum was readily detected under ambient conditions at the proper frequency (Fig. 3). However, the echo power predicted using Eq. 10 for the effective cross section was found to greatly exceed the level actually measured. The reason for the large difference is not clear, but it might stem from the coarseness of the initial theoretical approximations. The assumption of Fraunhofer conditions implies that the phase fronts of the refracted RF waves are planar throughout the common volume, and requires that the receiver be in the far field of this volume. Neither constraint is satisfied in the BWI configuration, but the role these factors play in the discrepancy remains unresolved. The limitations of time and scope have prevented further investigation.

As noted earlier, changes in the speed of the wavefronts, and thereby changes in the Doppler frequency, can be caused either by alterations in the local speed of sound or by the advection of the waves by air currents within the common volume. Both of these effects occur when a vortex wake descends into the field of view of the radar. In general, the change in Doppler frequency equals

$$\Delta f_d = -k_a(\Delta v_s + w), \tag{11}$$

where the perturbation in sound speed Δv_s depends on changes in temperature and composition, and w is the

THE CONNECTION BETWEEN SOUND PRESSURE LEVEL AND RADAR CROSS SECTION

Applying the assumptions and analysis in Ref. 2, the variable σ can be related to the change in index of refraction induced by the sound waves by

$$\sigma = (1/4\pi)k^4 V_C^2 (\Delta n_h)^2 \cos^2\theta_\sigma \, .$$

In this equation, $V_C \sim (x\beta)^3/\theta_s$ is the common volume defined by the RF transmitter and receiver beam patterns in Fig. 2, and k is the RF wavenumber. The term Δn_h is the amplitude of the index of refraction variations within this volume, which are represented as a train of plane waves,

$$\Delta n = \Delta n_h \cos[k_a(z - v_s t)] \, ,$$

where v_s is the sound speed and k_a is the acoustic wavenumber. The change in index of refraction can be related to the acoustic pressure by

$$\Delta n = K(\Delta\rho) = K(\Delta p)/v_s \, ,$$

where K (by definition) is the Gladstone-Dale constant and ρ is the air density. The acoustic pressure (Δp), in turn, is related to the intensity of the sound waves in the common volume by

$$\Delta p = 2(\Delta v_s) I \, ,$$

where the intensity is given by

$$I = [P_a g_a/(4\pi h^2)] \exp(-2\alpha h).$$

Here, P_a is the power of the acoustic source, g_a is the acoustic antenna gain, and h is the distance from the acoustic source to the center of the common volume. The variable α is the absorption coefficient, which depends on the acoustic frequency, the transport properties of air, and the relative humidity. For the range of altitudes and frequencies of interest in the present work, α is negligibly small, even at 100% relative humidity. The bracketed expression given in Eq. 9 in the text results from using the above relationships, with α set equal to zero.

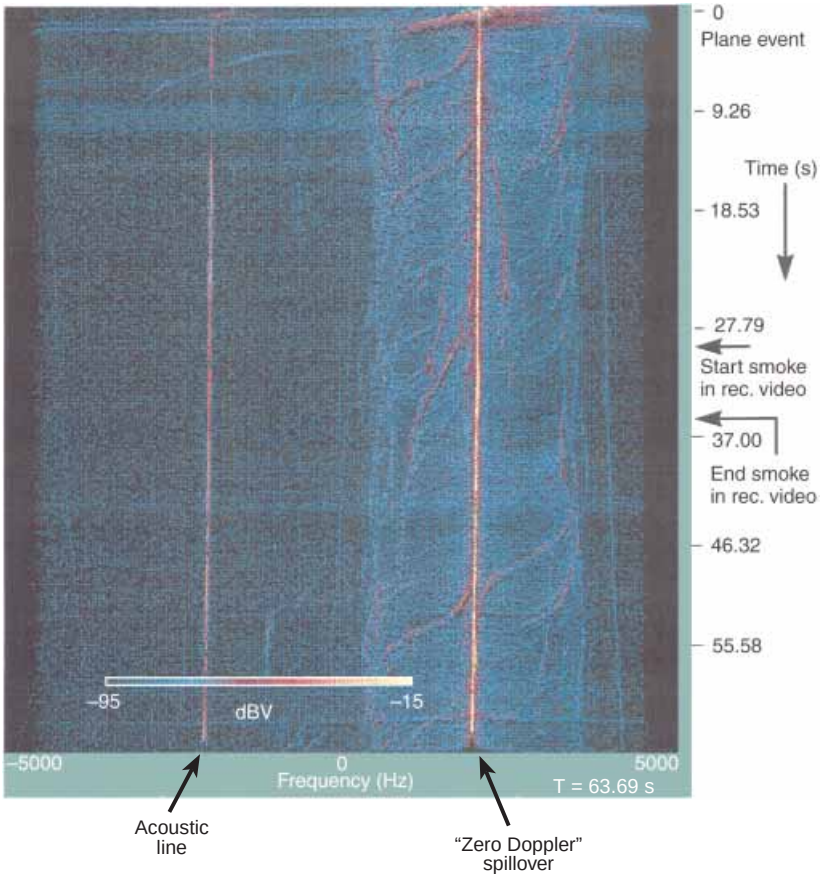

Figure 3. Spectrogram of run 9 on 29 October 1996 (10-kHz bandwidth).

component of the vortex velocity field parallel to the acoustic axis.

Because these variables are distributed nonuniformly, we might expect to see the Doppler spectrum broaden from a line to a continuous spectrum of width $(\Delta f_d)_{max}$ as the vortex wake moves into the common volume. This was not the case, however; observations showed a large signal dropout correlating with the arrival of the descending wake (see the Results section for a discussion).

PROCESSING

Receiver Processing

Figure 4 is a block diagram of the receiver processing. Both channels—the main vortex channel that is collecting information from the common volume (as well as spillover from sidelobes) and the reference channel—are mixed to approximately 25 kHz. From there, both channels are sent through a bandpass anti-alias filter. The data

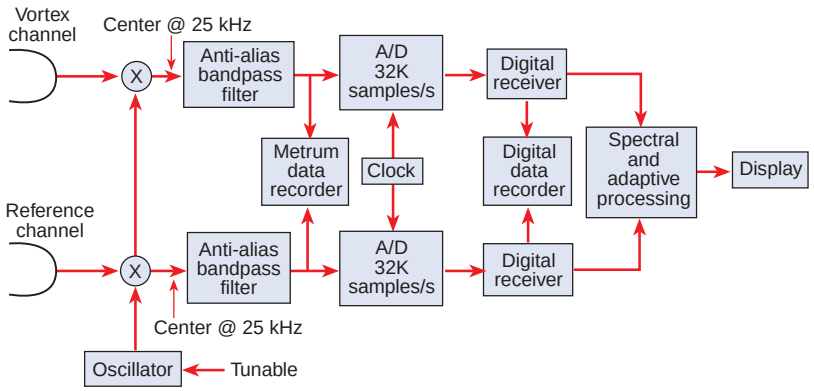

Figure 4. Receiver processing block diagram.

are then recorded on a Metrum RSR-512 rotary storage data recorder at an 80-kHz sampling rate and are sent for real-time data processing on a VME system at a sampling rate of 32 kHz. This latter rate, along with a downconversion/filtering scheme, will preserve up to 8 kHz of complex digital bandwidth, depending on which digital filter is used. All the digital filters are flat for approximately 75 to 85% of the passband, with out-of-band rejection greater than 90 dB. The four different digital filters, at ±4096, 2048, 1024, 512 Hz, use between 128 and 512 taps. From there, a time/frequency spectrogram is performed on the data, with a variety of time/frequency resolutions possible. The spectrogram, which is displayed in real time on a PC, is described next.

Spectrogram Processing and Display

Briefly, a spectrogram is a specific type of time/frequency distribution based on the periodogram, with extensions built in for time resolution. Many types of time/frequency distributions have received much attention; however, for real-time display, none can compare to the fast Fourier transform (FFT)-based distribution in terms of computational speed.

Figure 5 is a block diagram of overlapping FFT processing known as the spectrogram. After the digital receivers, the complex data are buffered. This allows the FFT to be overlapped by any desired amount. Three parameters control the spectral processing. (1) FFTsize is the size of the FFTs used (typically 256, 512, or 1024 points). (2) FFTdsize is the data size portion of the FFTsize. Typically, this is at most the FFTsize or 1 to 2 powers of 2 smaller. This parameter, along with the sampling rate and the specific digital filter used in the digital receiver, will establish the spectral resolution. If a windowing function is used, it may also affect the resolution. (3) FFTndsize is the new data size portion of the FFTdsize for FFT processing, which will typically be at most the FFTdsize or perhaps 1 to 4 powers of 2 smaller. This parameter will establish the time resolution of the spectrogram. In addition to these parameters, the noise floor parameter can be set to between −10 and −150 dB, and variable infinite impulse response-type averaging can be performed on the postmagnitude operation.

Figure 3 is an example of the spectrogram for run 9 on 29 October, with FFTsize = 1024, FFTdsize = 512, and FFTndsize = 128 in a digital bandwidth of ±5000 Hz. With these parameters set, along with a Hanning windowing scheme that reduces the spectral resolution, the spectral resolution is approximately 15 Hz. The time resolution is approximately 0.13 s, since this is the amount of spectral integration that occurs between successive FFTs. In Fig. 3, time progresses downward, where extent of the time scale is a function of the number of graphics pixels in the display window. With a 1024 × 768 display mode set, this window yields approximately 78 s of simultaneously viewable spectrogram data. The interpretation of the data will be discussed in the Results section.

Adaptive Processing

The spillover from the transmitter to the receiver is several orders of magnitude larger than any atmospherically based signal reflected down from the common volume. This makes any detections close to the zero-Doppler frequency difficult to obtain. To cancel some of the spillover, the reference channel is used to adaptively cancel anything that is common. Illuminator phase noise is common to both channels and thus should cancel, whereas the vortex signal, which is not contained in the reference channel, should become

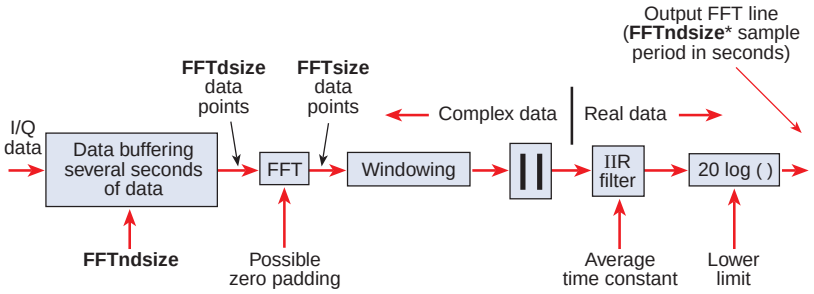

Figure 5. Block diagram of spectrogram FFT processing (IIR = infinite impulse response).

more apparent after adaptive processing. The formulation for this adaptive process assumes that the main vortex channel has two components: the common volume component and the direct spillover component. The reference channel is first phase-shifted and scaled to match the zero-Doppler magnitude and phase of the vortex channel peak, and then subtracted. The subtraction is performed in the frequency domain before the magnitude is taken. This has typically reduced the power in the zero-Doppler component in the main vortex channel by as much as 30 dB. Figure 6 is a block diagram of the adaptive processing, which can be contrasted to the spectrogram processing depicted in Fig. 5. Many runs were looked at with this process, and for those of importance on 29 October, adaptive processing was not needed since the returns were quite large.

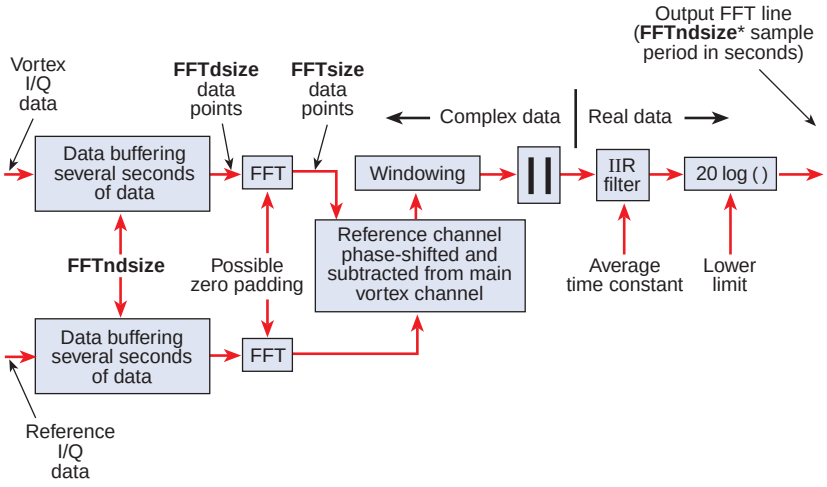

Figure 6. Block diagram of adaptive spectrogram FFT processing.

THE BWI EXPERIMENT

Both the Maryland Aviation Administration and the FAA where extremely helpful and receptive to the idea of allowing APL to install and operate the bistatic radar on the south side of runway 33L (Fig. 7). As mentioned previously, because of the proximity of the test site to a highway, wire screen fences (Fig. 8) were installed around both locations. This cut down reflections from cars as well as the direct path signal from the transmitter to the receiver.

The traffic interference can be recognized in waterfall spectra as a double S-shaped curve with an inflection point at zero Doppler (Fig. 3). This region of zero Doppler occurs when the vehicle is midway between the transmitter and receiver and the rate of change of the sum of the ray paths from the transmitter and the receiver to the vehicle is zero. At times prior to this there is a decreasing positive rate of change (positive Doppler); after the midway point there is an increasing negative Doppler. The maximum positive and negative velocity is limited to that of a monostatic radar with a completely radial component. Traffic interference can be seen in the actual waterfall data of Fig. 3 as depicted in Fig. 9.

Initial checkout of the system consisted of antenna alignment testing followed by measurement of receiver signal levels in clear air, both with and without acoustic pumping. Also, with the runway out of service, the acoustic transmitter was moved to several locations along its centerline, and receiver signal levels were monitored. During this phase of testing, the acoustic transmitter consisted of a Peavy 44T compression driver loaded with a 60° horn, which was typically driven with less than 20 W. A digital synthesizer was used to generate a sinusoidal input to the amplifier, which could be varied in frequency.

Tests confirmed that the optimal orientation of the acoustic source was vertical and directly in line between the transmitter and receiver along the centerline of the runway; i.e., at about 79 m from the south end of the runway. Unfortunately, commercial aircraft are at a very low altitude as they pass over this point, perhaps ≈50 m or less. At this altitude, a vortex can be unstable and dissipate quickly. To allow better control of the test environment, arrangements were made for a NASA C-130 aircraft from Wallops Island, Virginia, to overfly the runway on several days. These flights were funded by NASA as a contribution to the APL research efforts.

Test Aircraft

The C-130 aircraft was equipped with smoke generators (smokers) installed on both wingtips. The smokers burned corvus or canopus oil at the wingtip, which caused the smoke to became entrapped in the vortex core (see Fig. 10). The entrapped smoke allowed visual tracking of the otherwise invisible vortex. The right-tip smoker was inoperative for the first two test dates owing to a defective switch in the cockpit; however, both tip smokers were operational during the third and final test date.

Pretest instructions required the C-130 crew to fly the glide slope until reaching the requested altitude, which was to be held until the aircraft passed 305 m beyond the runway threshold. To conserve the corvus oil, the smoke was to be turned on 305 m prior to the

(a)

(b)

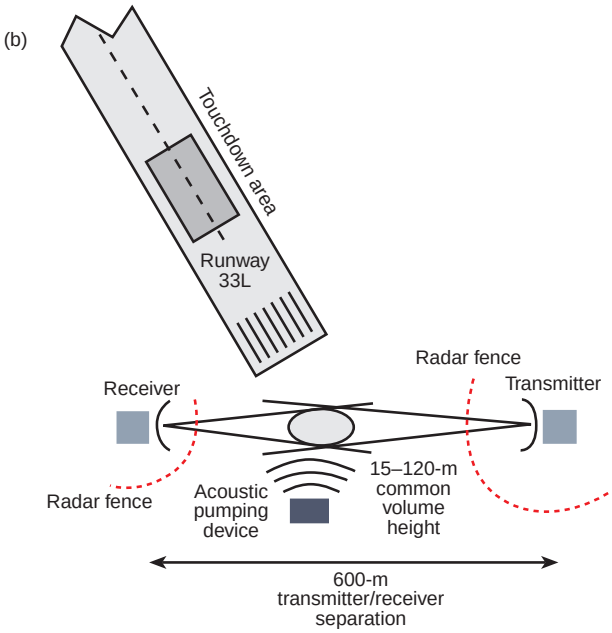

Figure 7. BWI vortex detection test site on runway 33L: (a) aerial photograph and (b) schematic view.

runway threshold and turned off 305 m beyond the threshold. A NASA video of the C-130 taken during a previous test at Wallops Island revealed that the tip vortices would break up if the landing flaps were used. Therefore, the C-130 was instructed to fly by the APL test sight in a "clean" configuration (gear and flaps up) at a speed of 1.3 Vso (120–130 kt). (Vso = stall speed or minimum steady flight speed at which the aircraft is controllable in the landing configuration.) At this speed and at maximum fuel weight, the strength of the vortices generated by the C-130 equaled that generated by a Boeing 727.

During the test, the C-130 received instruction via a UHF radio that was based at the radar receiver location. APL would transmit altitude and lateral displacement instructions to the crew before each flyby. The co-pilot received instructions from the APL test site, while the pilot communicated with the control tower at BWI.

Data Collection Procedures

A typical run of the C-130 involved at least six people: four at the receiver container, one at the transmit container, and one at the acoustic site. One person (local controller) was in voice communication with the C-130 at all times. The local controller and at least three other people were at the receiver container and would specify a height above the runway and distance from side to side offset from the runway to the crew. A "mark" would be given to the two or three people manning the receiver equipment that the C-130 was about 305 m out. Data collection usually started at this point. Visual contact was also made by the person voice-annotating the Metrum data. The receiver container, the transmit container, and the person manning the acoustic illuminator were all in radio communication. The person at the acoustic setup, which was in-line with the runway, would give a mark when the C-130 was over Dorsey Road and then when

Figure 8. Wake vortex receiver at BWI.

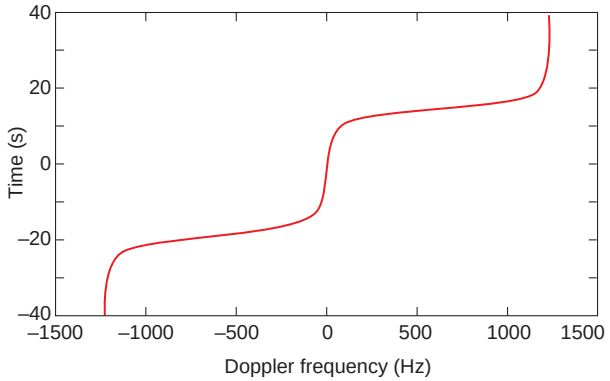

Figure 9. Interference shown for a vehicle traveling 40 mph on Rte. 176.

over the common volume. At this point, most of the voice annotation centered on the vortex smoke trails as seen by the receiver video camera. When the transmit container saw smoke in the transmit monitor, radio contact was made and notes taken at the receiver container specifying the degree of visual collaboration of smoke in the cameras at the receiver and transmit sites. This procedure worked well in establishing which of the many data runs were worth further investigation.

Observed Vortex Behavior

The behavior of the wingtip vortices was videotaped during the three test periods. Near-surface temperature and wind data were recorded at the radar receiver site. Recording devices were not allowed near or above the runway surface. Operations during the evening hours provided the most stable atmospheric conditions for the first test period. Because of the time change to Eastern Standard Time after the first tests and the heavy airline activity, the second and third tests were conducted during the morning and afternoon hours. A general description of the wind conditions and the vortex behavior during each test period is given in the following paragraphs.

The first test began at 5:20 p.m. on 23 September. Winds were 5 to 10 kt along the runway centerline. The C-130 made 20 passes by the APL test site at altitudes ranging from 15 to about 107 m above ground level (AGL). As noted earlier, the left wingtip smoker worked, but the right tip had malfunctioned. The left-tip vortex lasted more than 2 min after the C-130 flyby. The vortex remained near the runway centerline at approximately 12 m AGL. In some cases, the vortex passed through the boresight camera's view and would reappear shortly thereafter, giving the false impression that the vortex was rising. Instead, it remained near about 12 m AGL but underwent a wavelike oscillation. The peak of the wave motion reappeared in the boresight camera's view.

The first test date provided the best atmospheric conditions for vortex longevity, but posttest analysis determined that the radar's common volume was too low and the local traffic on Dorsey Road caused too much interference in the radar data.

(a)

(b)

Figure 10. The NASA C-130 research aircraft with generator on left wing. (a) Trailing vortex seen on approach to BWI. (b) Smoke-marked vortex as seen several seconds after the C-130 passed by (a).

The second test started at 9:50 a.m. on 29 October. Again, the right-tip smoker had malfunctioned. Initially, winds were approximately 15 to 20 kt across the runway. In some cases, the C-130 was instructed to fly at two wingspans about 80 m to the right of the runway centerline in hopes that the vortices would pass through the radar's common volume. After six passes, the winds decreased to light and variable and the C-130 was instructed to fly over the runway centerline. Fifteen passes were made by the C-130 until the BWI tower terminated testing owing to increasing commercial air traffic. The second half of this test provided the best radar data.

The third and final test date was 10 December. The malfunction in the right-tip smoker had been corrected, thereby allowing the observation of the interaction

between the left and right vortices. The C-130 was committed to a full day of testing, which included a landing at BWI with the smokers on. Wind conditions were less than ideal, with estimated crosswinds at velocities of 20 to 25 kt. Lateral positioning of the C-130 was difficult owing to the variation in the wind velocity and direction. Even under these conditions the tip vortices would remain intact for over 1 min. The vortices appeared in the boresight camera's view for only a few seconds because of the lateral displacement caused by the crosswinds.

Testing on 10 December began at 10:19 a.m. The C-130 made 13 passes before the BWI controllers terminated the test because of an increase in commercial air traffic. At this time, the C-130 landed for refueling with the smokers on. The tip vortices were destroyed within two C-130 body lengths, with the landing flaps fully deflected.

Afternoon testing began at 1:35 p.m. The winds had not subsided, and lateral positioning remained a problem. The radar's common volume was moved in an attempt to track the vortices as they were displaced by the crosswinds. At 3:00 p.m., the C-130 made its 40th and final pass of the afternoon and returned to Wallops Island.

RESULTS

No significant Doppler signatures could be correlated with the times and runs when smoke was seen in the video cameras on 23 September or 10 December. On the earlier date, the common volume was at 15 m, which we later realized was a poor choice because of ground effects. On 10 December, the winds made it difficult to impossible to position the C-130 so that smoke would drop through the common volume.

Two data runs taken on 29 October are detailed in the following paragraphs. Both proved to have definitive Doppler signatures when smoke was observed to be dropping through the common volume. (A more detailed presentation of the data from all the runs may be found in Ref. 11.)

The radioacoustic return showed a large signal dropout correlated with the arrival time of the descending wake (cf. Fig. 11a). The major qualitative difference between these results and the simplified picture presented earlier is likely due to a combination of effects associated with three phenomena:

1. Wake turbulence. Fluctuations in velocity and temperature distort the acoustic wavefronts, scattering the acoustic power and causing a loss of coherence in the wavetrain.
2. Cross-currents. Velocity components perpendicular to the acoustic axis tilt the Bragg grid, changing its geometry with respect to the RF beams, and possibly de-tuning the system.
3. Vertical shear. The presence of shear means that waves are advected by differing amounts in different parts of the wavetrain. When the acoustic axis is vertical, the fractional change in wavenumber along a central ray is directly proportional to $\partial w/\partial s$, i.e.,

$$\partial(\ln k)/\partial s = -\partial w/\partial s/(v_s + w), \qquad (12)$$

where s is the distance along the ray. The resulting refraction is strongest in the core region of the vortices and would tend to de-tune the system when the cores occupy the common volume.

Recall Fig. 3, a spectrogram of the data from the main vortex channel from run 9 (time running from oldest to newest, top to bottom). Figure 11b is a reduced bandwidth view of the same run. Here the frequency resolution is approximately 1 Hz as opposed to 15 Hz in Fig. 3. Marks have been added to the time axis where the smoke was observed in the cameras. A Doppler event within these marks is evident and is believed to represent the drop rate of the vortex core. The positive side of the Doppler spectrum corresponds to the "drop side" Doppler, i.e., the path length is being shortened. Calculations of the drop rate from the receiver video after the fact seem to generally agree with the drop rate indicated by the spectrogram and with the results of the numerical model calculations (cf. Fig. 15). Knowing the video camera's field of view and the approximate distance to the smoke, the video drop rate was estimated to range from 1.3 to 3.5 m/s. This corresponds to a Doppler frequency at the specific X-band frequency used of approximately 30 Hz (2 m/s).

Figure 11c is a cut through the spectrogram at the time when the vortex signature was the strongest. From this figure, the estimated Doppler offset is approximately 40 Hz. Two other traces are depicted here, attempting to place bounds on C_n^2 using different measurement methods. The top trace (upper bound) assumes that the full common volume (about 1000 m^3) is contributing to C_n^2, and the energy is concentrated in the narrow frequency band of the vortex signal shown in the figure. The bottom trace (lower bound) assumes that the received energy is spread over the frequency band corresponding to the estimated turbulent velocities contained in the vortex. The figure shows that C_n^2 is several orders of magnitude greater than the upper bound, suggesting that vortices may have C_n^2 values much greater than expected for strong, clear air turbulence. Another explanation is that the smoke contained in the vortex is contributing to overall vortex reflectivity. Compare Fig. 11c with Fig. 11a, a peak amplitude versus time plot for the acoustic line. Here, the dropout from the passage of the plane is apparent; however, little else could be counted on because of the wide swings in received power.

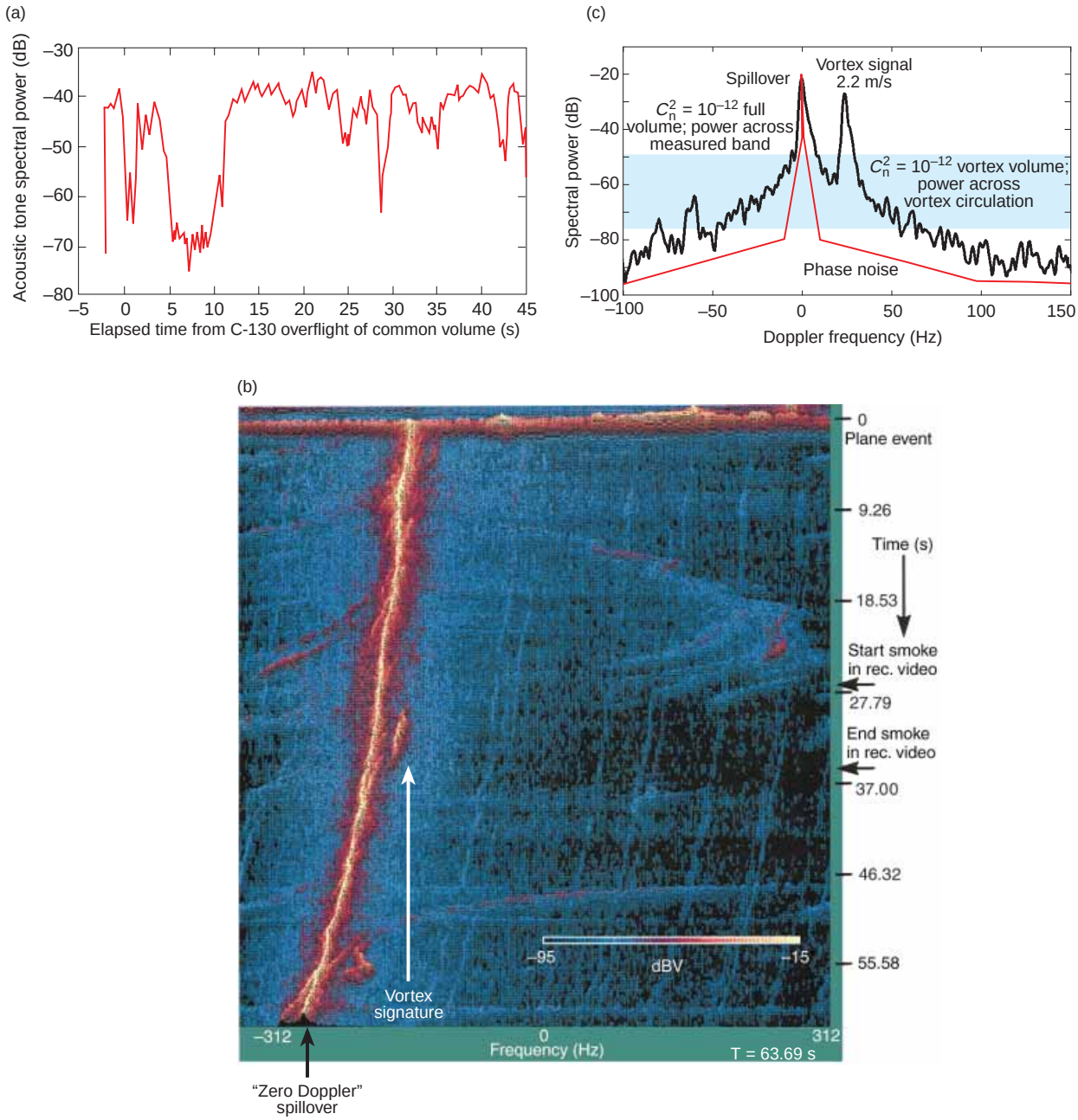

Figure 11. Run 9 on 29 October 1996: (a) acoustic line power, (b) spectrogram, and (c) single line through spectrogram.

Figure 12 shows the acoustic amplitude, spectrogram, and single line spectrum for run 15. Again, the reader will find details on additional runs in Ref. 11.

MODEL PREDICTIONS OF AIRCRAFT VORTEX WAKES

Model calculations have been carried out for runs 9 and 15 from 29 October. Our objectives were (1) to determine the extent to which the model could predict the early evolution (prior to breakup) of aircraft vortices and (2) to help interpret the radar measurements described in previous sections.

Obviously, some success in model validation is required if the model is to be used to provide estimates of the location, strength, and internal structure of the atmospheric flow signatures believed to be responsible for the measured radar returns. Accordingly, our approach was to first examine the predicted wake vortex trajectories and then to compare the predicted time of arrival of the vortex cores at the radar common volume with the time at which radar signatures were observed. Since no ground-truth measurements of atmospheric motions were available during the BWI experiment, these were the only comparisons that could be used to help establish the model's credibility. The next step in

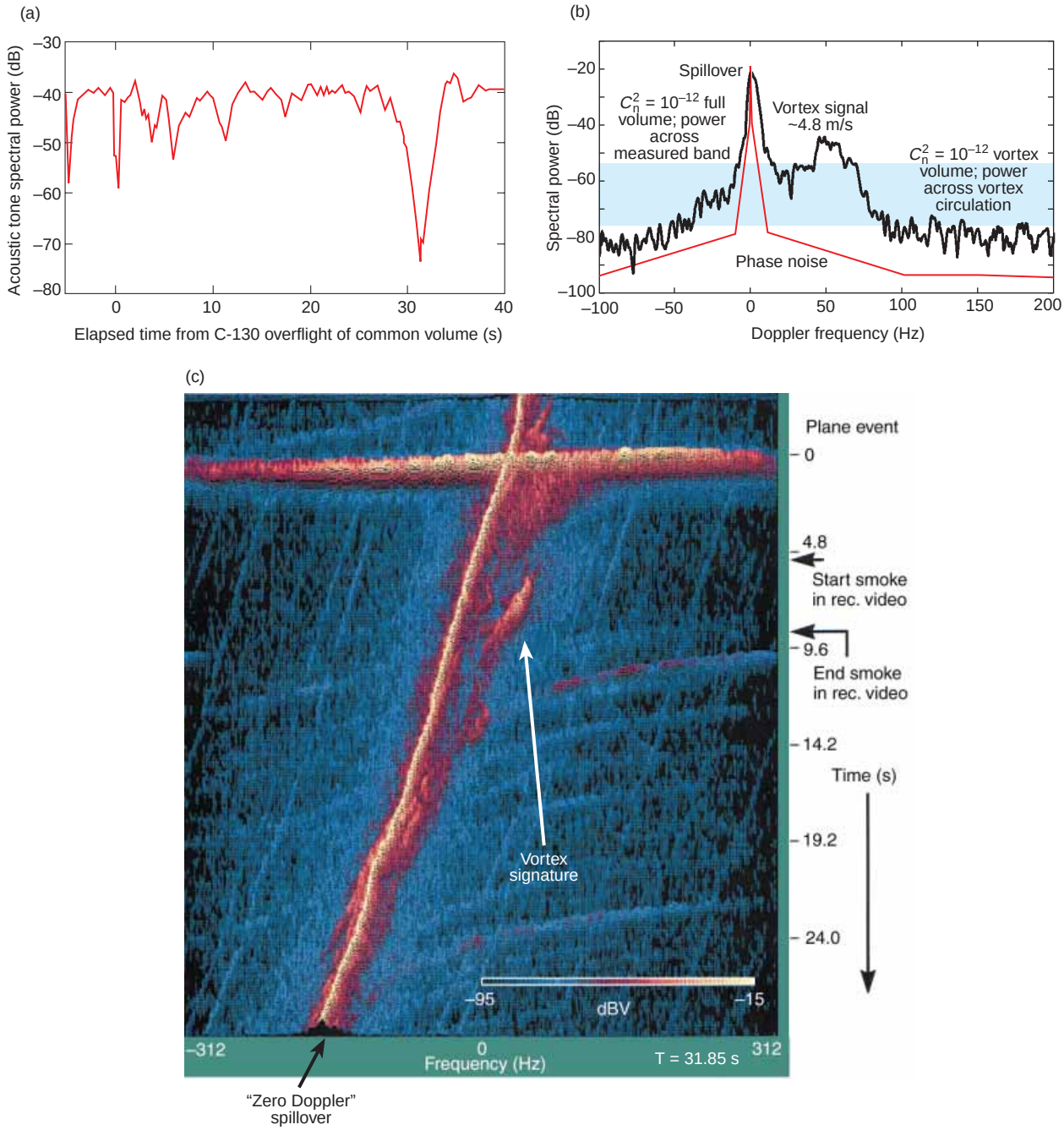

Figure 12. Run 15 on 29 October: (a) acoustic line power, (b) spectrogram, and (c) single line through spectrograph.

the analysis process was to examine features of the predicted vortex wakes (e.g., overall size, internal structure) to better understand what parts of the signature might be responsible for the measured radar returns.

Predictions of vortex wake evaluation were obtained using the recently developed APL Wake Evaluation Code (AWEC). AWEC solves steady-state nonlinear equations for the velocity $\vec{V}$, density ρ, turbulence kinetic energy K, and turbulence dissipation rate ϵ, all in a coordinate system that is fixed with respect to a moving source (in this case, an aircraft) and moves linearly with that source. A second-order turbulence closure scheme, based largely on the Mellor and Yamada Level 2.5 model,[12] is used to evaluate the remaining turbulence correlations.

The principal approximation in AWEC, and the one that renders the problem tractable, is the so-called parabolic approximation. The physical assumption behind this approximation, which is valid for almost all wake flows, is that changes in the downtrack or x direction are small compared with changes in the crosstrack and vertical (y and z) directions. Derivatives of x other than those in advective terms involving the

mean speed of advance U are neglected, thereby allowing the equations to be reformulated and solved as a marching problem in x. The need to store model variables at locations along the x axis is eliminated, thus reducing the problem from three to effectively two spatial dimensions.

To initialize AWEC model calculations, estimates of data are needed at a vertical (y–z) plane close to the origin. For submarine wake predictions, a separate program, FWI,[13] is used to generate estimates of component wakes for the many sources that contribute to the composite wake signature. FWI stores relevant geometrical variables for different submarines and uses these values along with operating conditions provided by the user to compute estimates for variables such as the size and strength (circulation) of vortices shed by the hull and control surface. For the present aircraft vortex calculations, it was a fairly straightforward exercise to add a file containing the wingspan and other relevant geometrical variables for a C-130 transport and to use existing software to calculate the required initial plane data. Since the inviscid theory applied to derive the vortex circulation equations in FWI was originally developed for the aircraft vortex problem, there was little risk in applying those same equations to the problem at hand. And since, unlike submarine wakes, aircraft wakes are dominated by a single component, all sources other than wing vortices could safely be ignored.

Run 9

During run 9, the aircraft was assumed to be in level flight at an altitude of 83.8 m, with an air speed U of 64.3 m/s. The plane's weight was taken to be 143,000 lb (64,865 kg), and the lift force L was assumed equal and opposite to the weight. The wingspan B was about 40.4 m.

The initial vortex circulation Γ_0 was estimated from the inviscid theory. Assuming elliptical loading,

$$\Gamma_0 = \frac{L}{\rho U b_0} = 312 \text{ m}^2/\text{s} \quad , \tag{13}$$

where the density of air ρ = 1 kg/m^3, and the vortex core separation b_0 is given by

$$b_0 = \frac{\pi}{4} B = 31.7 \text{ m} . \tag{14}$$

The diameter of the vortex core D_V is given theoretically by

$$D_V = 0.197 b_0 , \tag{15}$$

which yields an estimate of D_V = 6.25 m for the C-130. This value was considerably larger than the observed core diameter of approximately 1 m. The latter value was determined by the visible boundary of the entrained smoke in the photographs. Despite this discrepancy, the larger theoretical value was used in the model calculations. Use of the smaller value would have required a minimum grid separation distance much smaller than the 0.5 m used in the present calculations, which would have resulted in a nearly prohibitive increase in the computational burden.

The net downward vertical velocity w_0 induced by one vortex acting on another is given by

$$w_0 = \frac{-\Gamma_0}{2\pi b_0} = -1.57 \text{ m/s} . \tag{16}$$

The atmosphere was assumed to be weakly stratified with a potential temperature gradient of 6.7 $\times$ 10^{-3} °C/m. Values of potential temperature were converted to density for use by AWEC. Ambient levels of turbulence kinetic energy and turbulence kinetic energy dissipation rate were chosen to be 0.1 m^2/s^2 and 2 $\times$ 10^{-3} W/kg, respectively.

Figure 13 depicts vector velocities at times late t of 1.4 (the initial plane), 9.0, 21.0, and 31.0 s. Since the wing was positioned near the top of the fuselage (effective diameter of approximately 5.2 m) on the C-130, the vortex cores initially were situated 86.4 m AGL. Figure 14 shows contours of the turbulence kinetic energy for two of these times late, 1.4 and 31.0. The position of the radar common volume, which is centered at 45.7 m AGL, is also shown.

Figure 15a plots the position of the vortex cores (solid curve) as a function of t. The heavy dashed line indicates where the vortex positions would be if the wake descended at a constant velocity given by the induced velocity computed from Eq. 16. The actual vortex descent begins near this speed but then slows. The fixed upper and lower boundaries of the common volume are indicated by a pair of solid horizontal lines. The outlying lighter dotted lines indicate the first contour level above ambient of the turbulence kinetic energy distribution.

From Fig. 15a it is estimated that the leading edge of the vortex wake first reached the common volume approximately 12 s after aircraft passage and that the vortex cores were within the common volume between $t \approx$ 29 and 33 s after aircraft passage. Radar results discussed previously show a distinct signature at t = 31 s, which appears consistent with the model prediction. This result, however, could be fortuitous as it depends on the aircraft altitude at the time of passage, and there is considerable uncertainty in the estimates of altitude obtained from the C-130 pilot.

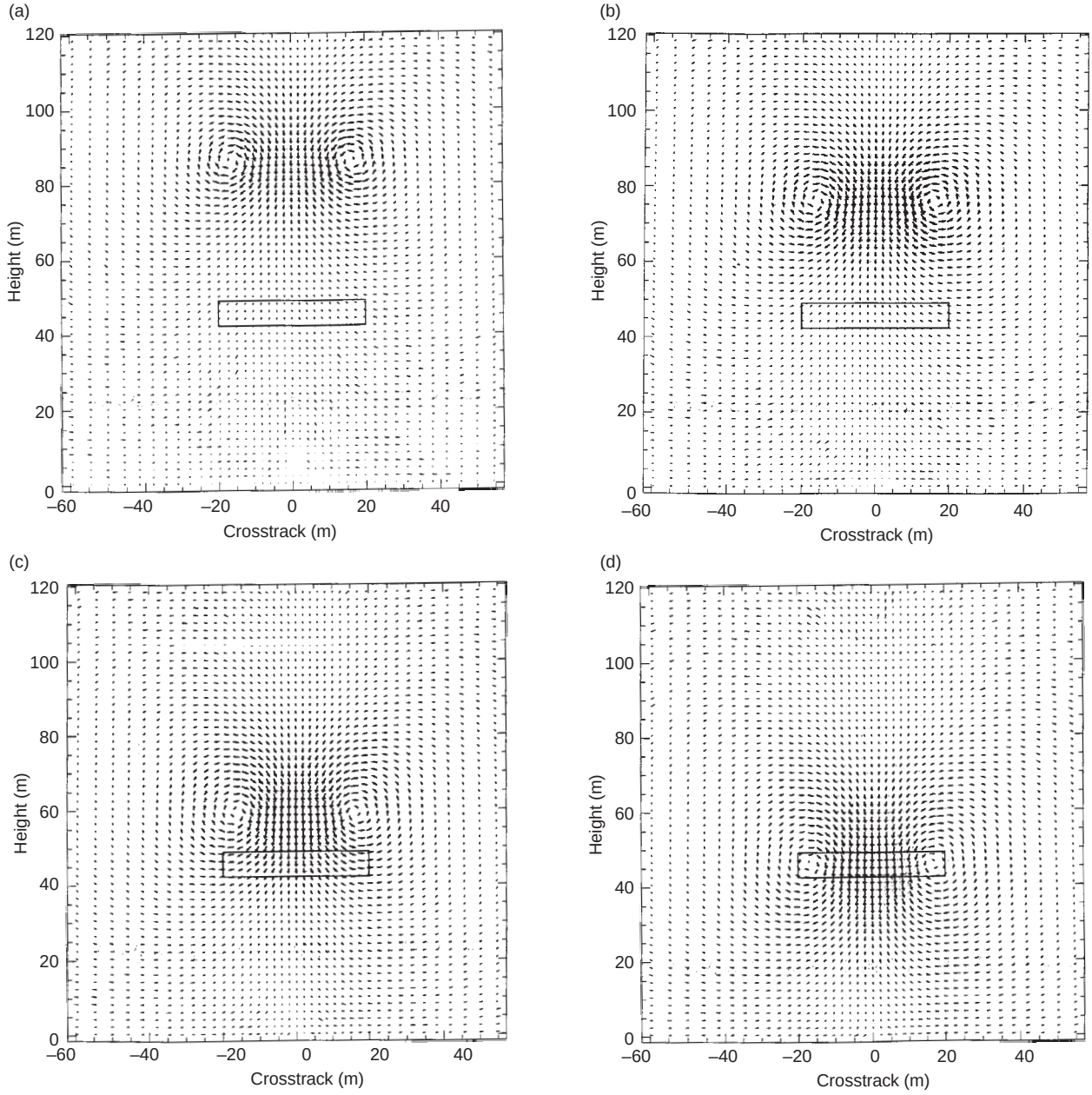

Figure 13. Run 9 vector velocities at times late of (a) 1.4 s, (b) 9.0 s, (c) 21.0 s, and (d) 31.0 s.

Run 15

Except for the altitude, all model inputs for run 15 were the same as those for run 9. Although the reported altitude was 64 m, a video tape of the aircraft flying over the common volume shows that the vortex cores as measured by smoke are in the common volume at the time of passage. Accordingly, an initial vortex-core height of 53.3 m was adopted for the run 15 model calculation, which resulted in better agreement with experimental data.

Figure 15b plots the position of the vortex cores as a function of time. Again, the actual vortex motion descent rate is slower than predicted by inviscid theory. Vortex cores are predicted to be within the common volume between 6 and 12 s after aircraft passage. This agrees with the radar observations—an expected result here since the radar data along with the video were used to estimate the initial altitude.

DISCUSSION

Radio waves are scattered by turbulent irregularities in the refractive index of air. In the initial stages of a turbulent mixing process, air parcels are rapidly displaced from each other and their identities are preserved. It takes a while for diffusion to act and for the mixed region to become nearly homogeneous again. The stronger the initial gradients and the turbulence,

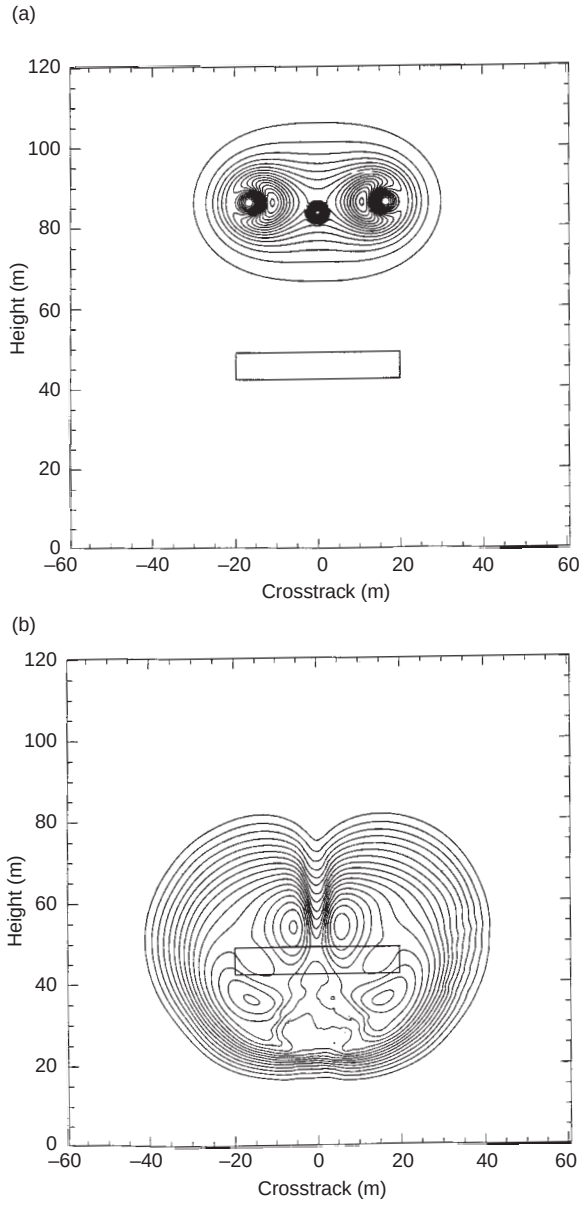

Figure 14. Contours of turbulence kinetic energy for run 9 at times late of (a) 1.4 s, and (b) 31.0 s.

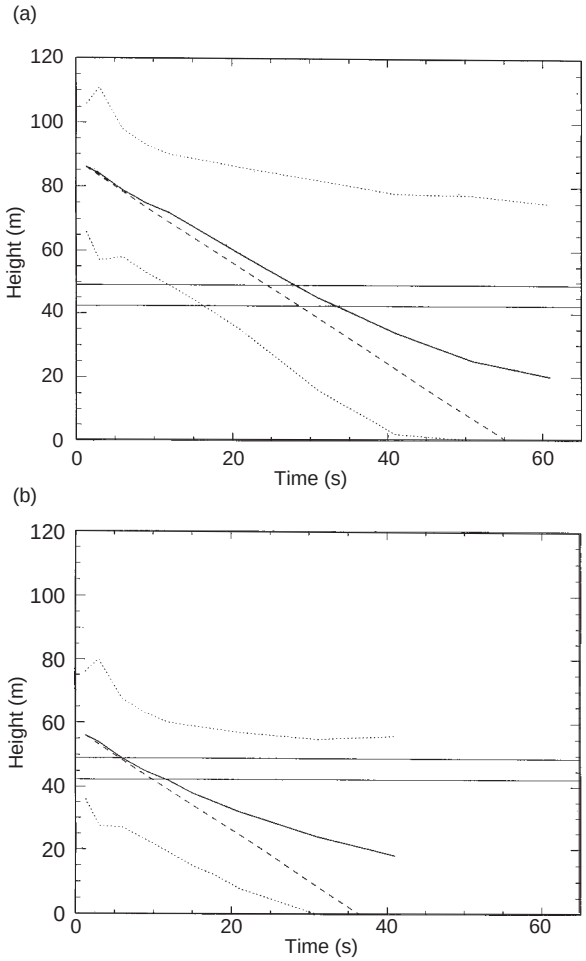

Figure 15. Vortex trajectories for (a) run 9 and (b) run 15. The position of the vortex cores (solid curve) is plotted as a function of time late. The heavy dashed line indicates where the vortex positions would be if the wake descended at a constant velocity given by the induced velocity computed from Eq. 16. The actual vortex descent begins near this speed but then slows. The fixed upper and lower boundaries of the common volume are indicated by a pair of solid horizontal lines. The outlying lighter dotted lines indicate the first contour level above ambient of the turbulence kinetic energy distribution.

the larger are these temporary local variations in the refractive index.

The physical variable most identified with radar signatures is the structure parameter C_n^2 discussed previously. To effectively use the model predictions to interpret the radar observations, a means must be found to relate C_n^2 to the mean-flow and turbulence variables predicted by AWEC.

An algebraic expression for C_n^2 in terms of selected AWEC model variables has been derived for a special case of zero moisture content in the atmosphere,[11]

$$C_n^2 = \frac{a^2}{\varepsilon^{1/3}} \frac{(77.6R)^2}{10^4} \left(-\overline{\rho' v'} \frac{\partial \rho}{\partial y} - \overline{\rho' w'} \frac{\partial \rho}{\partial z} \right), \quad (17)$$

where ε is the turbulence dissipation rate, $\overline{\rho' v'}$ and $\overline{\rho' w'}$ are turbulence density-velocity correlations, and $\partial\rho/\partial y$ and $\partial\rho/\partial z$ are gradients of the mean potential density[14] in the horizontal (cross-track or y) and vertical directions, respectively. Constants appearing in Eq. 17 are the universal gas constant R and a^2, which ranges between 0.4 and 4. A value of $a^2 = 1.0$ was chosen for estimating C_n^2 in this study.

Figure 16a shows that the wake boundary as determined by the structure parameter roughly coincides with the outer contour of turbulence kinetic energy for run 15, which is shown for comparison in Fig. 16b. Unlike the turbulence kinetic energy, however, the plot of C_n^2 shows evidence of structure within the vortex wake. Values of C_n^2 range from -30 to -70 dB over the extent of the recirculation cell, with the

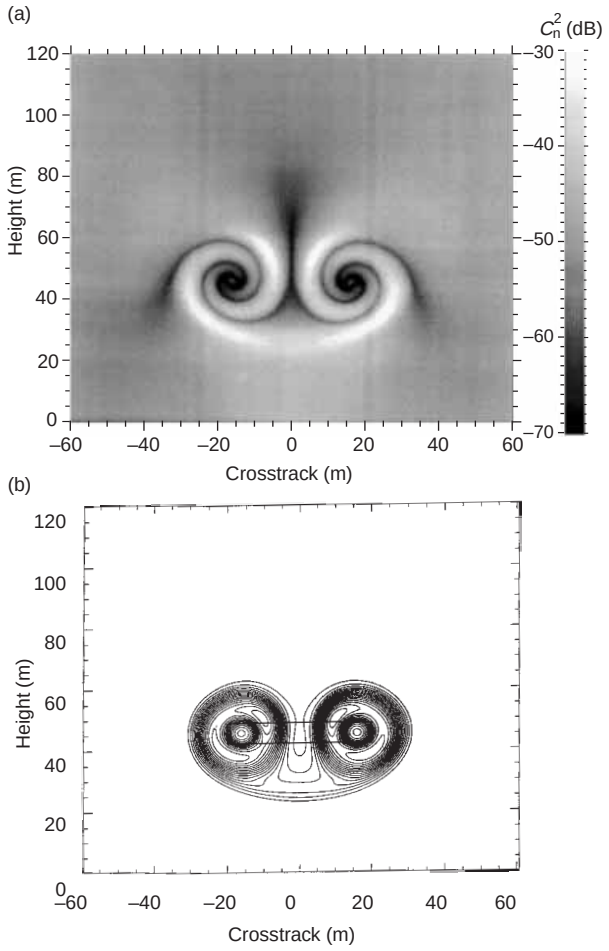

Figure 16. Run 15 at 9.0-s time late: (a) gray-scale plot of C_n^2 and (b) contours of turbulence kinetic energy.

largest values occurring near the vortex cores. The plot of C_n^2 also shows a well-defined leading edge of the wake.

It is unclear whether mean velocities (as measured by the vector plots) or turbulent perturbations to the refractive index (as measured by the structure parameter) are primarily responsible for the observed radar signatures. The coincidence of regions of high velocity with regions of high C_n^2 in the model predictions makes it difficult to use model predictions to resolve this issue.

The interpretation of the radar measurements is also made difficult by the absence of ambient crosstrack wind data. The model predictions, which assumed no ambient wind, show most of the vortex wake (including both cores) passing through the radar common volume; however, even a modest crosstrack wind could cause an offset that could result in only one of the cores being detected. In the former case, the large rotational velocities would likely be averaged out, leaving only the much smaller (≈1 m/s) net downward-migration velocity to be measured. In the latter case, the radar could be detecting the composite of the vortical velocity and the migration velocity, which, according to the model predictions, could be as high as 7.4 m/s in regions where the two components add. Clearly, future experiments would benefit by direct measurements of the atmospheric variables of interest.

SUMMARY

APL has designed and constructed a bistatic continuous-wave radar system for experimentation in aircraft wake vortex detection. Many hurdles, both technical and logistical, were overcome in developing the facility. Acoustic pumping was evaluated as a possible technique to enhance overall detection performance. The radar and acoustic systems were installed at BWI in the fall of 1996, and controlled experiments using a NASA C-130 aircraft were conducted.

From these experiments, Doppler signatures from the main vortex signal were found in several data runs. The acoustic signal showed amplitude dropouts that coincided with the passage of the aircraft through the common volume and could be used for a coarse, but unreliable, detection of vortex passage. We speculate that with the wider-band acoustic illumination, Doppler phase modulations will also be visible.

APL has carried out a number of wake vortex simulations in support of these experiments. Model results have been used to help interpret the data observations. Predicted vortex trajectories were found to agree with the data when uncertainties in the aircraft altitude were taken into account. The model predictions have also provided insight into which part of the overall wake signature might be producing the observed radar returns.

The main result from these experiments is that vortices are detectable with the APL X-band bistatic radar system. In addition, given the tremendous volume that must be scanned in an operational environment, the current system parameters (power, resolution) appear to be more than suitable for a fieldable vortex detection radar.

One possible future direction would be to add the ability to track vortices in and around the end of the runway. This, along with a search mode, would be required to make the current radar a valuable sensor in an operational environment. Another possibility would be to add a millimeter-wave radar, since modeling has shown that it may be possible to observe intercore velocities with shorter wavelengths. Finally, we would like to extend our experimentation with various acoustic waveforms and techniques to further our understanding of the radioacoustic effects.

REFERENCES

[1] Hanson, J. M., and Marcotte, F. J., "Aircraft Wake Vortex Detection Using Continuous-Wave Radar," *Johns Hopkins APL Tech. Dig.* 18(3), 348–357 (1997).

[2] Doviak, R., and Zrnic, D., *Doppler Radar and Weather Observations*, 2nd Ed., Academic Press, San Diego, CA (1993).

[3] *Measurement of Atmospheric Parameters with a Bistatic Radar Supplemented by an Acoustic Source*, Environmental Surveillance Technology Programme, Oslo, Norway (Oct 1995).

[4] Stewart, E. C., *A Study of the Interaction Between a Wake Vortex and an Encountering Airplane*, AIAA Paper 93-3642, Atmospheric Flight Mechanics Conference, Monterey, CA (Aug 1993).

[5] Smith, P. L., Jr., *Remote Measurement of Wind Velocity by the Electromagnetic Acoustic Probe*, Midwest Research Institute, Kansas City, MO (1961).

[6] Marshall, J. M., Peterson, A. M., and Barnes, A. A., Jr., "Combined Radar-Acoustic Sounding System," *Appl. Opt.* 11(1), 108–112 (Jan 1972).

[7] Frankel, M. S., and Peterson, A. M., "Remote Temperature Profiling in the Lower Troposphere," *Radio Sci.* 11(3), 157–166 (Mar 1976).

[8] Kon, A. I., "A Bi-Static Radar-Acoustic Atmospheric Sounding System," *Izvestiya* (Atmospheric and Ocean Physics) 17(6), 481–484 (1981).

[9] Kon, A. I., "Signal Power in Radioacoustic Sounding of a Turbulent Atmosphere," *Izvestiya* (Atmospheric and Ocean Physics) 20(2), 131–135 (1984).

[10] Kon, A. I., "Combined Effect of Turbulence and Wind on the Signal Intensity in Radioacoustic Sounding of the Atmosphere," *Izvestiya* (Atmospheric and Ocean Physics) 21(12), 942–947 (1985).

[11] Iannuzzelli, R. J., Marcotte, F. J., Hanson, Jr., J. M., Manzi, L. P., Schemm, C. E., et al., *Final Report: Results of the APL Bistatic X-Band Vortex Detection Radar from C-130 Flyovers at BWI Airport*, JHU/APL, Laurel, MD (1997).

[12] Mellor, G. P., and Yamada, T., "Development of a Turbulence Closure Model for Geophysical Fluid Problems," *Rev. Geophys. Space Phys.* 20, 851–875 (1982).

[13] Rosenberg, A. P., *FASTWAKE Initialization and Flow Evolution Program User's Guide*, STD-R-1577, JHU/APL, Laurel, MD (Nov 1987).

[14] Gill, A. E., *Atmosphere-Ocean Dynamics*, Academic Press, New York (1982).

ACKNOWLEDGMENTS: The authors gratefully acknowledge the contributions of Robert Neece and Ann McKenzie, NASA, Langley, C-130 funding; Doug Young and the C-130 crew at NASA, Wallops Island; Ben Martinez, MAA, BWI; and Jerry Dudley, FAA, BWI. The BWI experiment would not have been possible without the diligent efforts of Bernie Kluga and Bob Geller and the air traffic controllers of the FAA at the BWI Tower.

CONTRIBUTORS

(Back row, left to right) David A. Frostbutter, William R. Geller, Laurence P. Manzi.
(Front row, left to right) Charles E. Schemm, Harold E. Gilreath, Russell J. Iannuzzelli, James M. Hanson, Jr., Frank J. Marcotte, Dennis L. Kershner, Alexander S. Hughes, Allen J. Bric, Bernard E. Kluga. Leo E. McKenzie is not pictured.